Lithium trithiocarbonate as a dual-function electrode material for high-performance lithium-sulfur batteries

*Hyunki Sul, Amruth Bhargav, and Arumugam Manthiram**

Hyunki Sul, Amruth Bhargav, Prof. Arumugam Manthiram
Department of Mechanical Engineering & Texas Materials Institute, The University of Texas at Austin, Austin, TX78712, USA
E-mail: manth@austin.utexas.edu

Keywords:
Lithium-sulfur batteries, trithiocarbonate, electrode materials, full cell, electrochemistry

Abstract: The development of practical lithium-sulfur (Li-S) batteries with prolonged cycle life and high coulombic efficiency is limited by both parasitic reactions from dissolved polysulfides and mossy lithium deposition. To address these challenges, we employ here lithium trithiocarbonate (Li_2CS_3)-coated lithium sulfide (Li_2S) as a dual-function cathode material to improve the cycling performance of Li-S batteries. Interestingly, at the cathode, Li_2CS_3 forms an oligomer-structured layer on the surface to suppress polysulfide shuttle. The presence of Li_2CS_3 alters the conventional sulfur reaction pathway, which is supported by material characterization and density functional theory (DFT) calculation. At the anode, a stable *in-situ* solid electrolyte interphase (SEI) layer with a lower Li-ion diffusion barrier is formed on the Li-metal surface to engender enhanced lithium plating / stripping performance upon cycling. Consequently, the obtained anode-free full cells with Li_2CS_3 exhibit superior capacity retention of 51% over 125 cycles, whereas conventional Li_2S cells retain only 26%. This study demonstrates that Li_2CS_3 inclusion is an efficient strategy for designing high energy density Li-S batteries with extended cycle life.

1. Introduction

The emergence of rechargeable batteries has aided substantial advancement in technology and mobility over the last decade. It is also replacing the power generation sources from fossil-fuel-based to renewable energy source-based, such as solar and wind energies.[1] Recently, due to the increasing demand for portable electronics and electric vehicles, traditional lithium-ion batteries make it challenging to meet the need for low-cost and high-energy density batteries.[2] Among the various alternative systems, lithium-sulfur (Li-S) batteries are gaining attention as a promising next-generation system, owing to their high theoretical specific capacity (1672 mA h g^{-1}), high energy density (2600 W h kg^{-1}), and low cost of elemental sulfur.[3,4] Regardless of the considerable advantages, there are several demanding problems in the cathode and anode that prohibit the practical application of the Li-S batteries.

The problems in the sulfur cathode include the following: (i) the low electronic conductivity of sulfur and its discharged products (Li_2S_2 / Li_2S) leads to poor utilization of active material and degradation in rate capability; (ii) a severe volume change (80 %) in sulfur during cycling results in a destruction of the cathode integrity and a rapid capacity fade; and (iii) higher-order polysulfides (Li_2S_n, $4 \leq n \leq 8$) dissolved into the organic electrolyte are also problematic since they can migrate to the anode and degrade the Li-metal. This so-called polysulfide shuttle effect results in an irreversible loss of active materials, low coulombic efficiency, and short cycle life.[5] To address the issues in the cathode, various approaches have been explored. Incorporating the insulating sulfur into conductive carbon frameworks facilitates electron transport between the active material and the current collector.[6–10] Highly porous carbon accommodates the volume change and enhances the structural integrity. Organosulfur compounds are another promising strategy owing to their enhanced reaction kinetics during discharge and reduced solubility in the electrolyte, which can mitigate the

parasitic shuttle effect.[11–13] Furthermore, organosulfur species can improve active material utilization by reducing the formation of insulating and passivating Li_2S layers upon discharge.

Beyond the issues with the sulfur cathode, the Li-metal anode suffers from a number of challenges: (i) the low reduction potential of Li causes corrosive reactions with most organic solvents, which not only forms an unfavorable solid-electrolyte interphase (SEI) layer that hinders Li-ion diffusion,[14] but also leads to a depletion of the electrolyte; (ii) inhomogeneous growth of Li-metal induces a severe safety risk of penetrating the separator and short-circuiting the cell;[15] and (iii) the migration of dissolved polysulfides causes parasitic reactions and corrosion at the anode, consumes active material, and polarizes the anode by precipitating insoluble Li_2S and Li_2S_2 on the Li-metal surface.[16] Strategies to resolve the problems with the Li-metal anode include structural modification of anodes such as coating of Li powder on the current collector[17] and generating micro-structured anode surfaces.[18,19] These processes increase the reaction sites for Li plating / stripping, subsequently preventing dendritic growth of Li. An alternative method is to form an artificial protective layer on Li-metal surface. Recently, it has been shown that the formation of a ternary sulfide ($Li_aX_bS_c$)-rich SEI layer significantly improves the Li plating / stripping efficiency.[20,21] Compared to the conventional binary sulfide (Li_2S/Li_2S_2)-rich SEI layer, layers containing ternary sulfides, such as Li_2TeS_3 or Li_3PS_4, have higher ionic conductivity and a lower Li-ion diffusion barrier, enabling a uniform Li-ion flux. The enhanced Li plating / stripping effect was reflected in the prolonged cycle life of anode-free full cells and symmetric cells.

Despite the novelty and effectiveness of the above-mentioned approaches, the most effective strategy to increase the practicality of Li-S batteries is to improve the performance of both the anode and cathode simultaneously. Several electrolyte-based methods have been suggested to act as not only a cathodic redox mediator but also to form a protective layer on the anode.[22,23] Gu *et al*. reported carbon disulfide (CS_2) as an electrolyte additive that can react with polysulfides and induce the formation of thiosulfate-containing protective layers on

both the anode and cathode.[24] These protective layers not only suppress polysulfide shuttle by forming complexes with polysulfides at the cathode, but also improve Li-metal morphology at the anode. However, the reason for thiosulfate SEI layer stabilizing the Li-metal anode and the reaction mechanism between polysulfides and CS_2 were not entirely elucidated. Also, even though the dual-functional electrolyte modification is promising, co-solvent amount of CS_2 hampers the redox kinetics, resulting in a degraded rate performance.

In this work, our motivation is to explore a cathode material that can simultaneously stabilize the anode and the cathode. Previous work has suggested that alkali-metal trithiocarbonates can serve as a surface passivating agent to prevent the Li-metal corrosion in Li-ion batteries.[25] It is also known that the trithiocarbonate exhibits strong interaction with both sulfur and polysulfide to suppress the shuttle effect.[26] Herein, we demonstrate enhanced cyclic stability and electrochemical performance by implementing lithium trithiocarbonate (Li_2CS_3)-coated Li_2S as a cathode material. An anode-free full cell and Li-metal half cell configurations are applied to evaluate the impact of Li_2CS_3 at both cathode and anode. Li_2CS_3 has several appealing features, including high discharge voltage, formation of an oligomer-structured layer on the cathode surface that suppresses polysulfide shuttling, and an improved anode morphology upon cycling. A unique reaction mechanism is suggested with density functional theory (DFT) calculations to provide supporting evidence.

2. Results and discussion

Alkali-metal trithiocarbonate have been used for the removal of heavy metals in wastewater treatment for decades. Trithiocarbonates are formed from the reaction of carbon disulfide and other sulfide sources. Li_2CS_3-coated Li_2S composite (hereafter referred to as Li_2CS_3 @ Li_2S) was synthesized by simply reacting Li_2S and an excess amount of CS_2 in a 1 : 3 mole ratio. Since Li_2S is a solid powder and CS_2 is in liquid state, wet ball-milling method was employed to realize a homogeneous reaction in 1,3-dioxolane / 1,2-dimethoxyethane

(DOL / DME, 1:1 vol.) as the slurry medium (**Figure 1a**). The synthesized compound was collected after drying the slurry to remove the solvent and excess CS_2. The synthesized Li_2CS_3 @ Li_2S powder was an orange-yellow crystalline compound as reported in the literature,[27] which is distinctive from the white colored Li_2S powder. The surface morphology change from granular shaped Li_2S (particle size of 500 nm ~ 1 μm) to a rough and chunky Li_2CS_3 @ Li_2S (particle size of 6 ~ 10 μm) (**Figure S1**) clearly indicated that the chemical transformation occurred largely on the surface. To investigate the surface chemistry of the synthesized compound, Fourier transform infrared spectra (FTIR) was employed (**Figure 1b).** The strong absorbance corresponding to the carbon-sulfur resonance bond was detected at 905 cm^{-1}, as observed in the literature, representing the formation of Li_2CS_3.[27] Small peaks of C – S stretching (located at 660 cm^{-1})[28–30] and C = S stretching (at 1073 cm^{-1})[31–33] are also seen in the spectra. The main source of C – S and C = S is from the reaction of Li_2S, CS_2, and lithium persulfide (Li_2S_2) (**Figure 1a**). Li_2S_2 is inherently present in the commercial Li_2S powder, which intrinsically contained ~ 8 mol% of the lower order polysulfides as an impurity as shown in **Figure 1d**. In order to distinguish the synthesized Li_2CS_3 @ Li_2S from CS_2, ^{13}C nuclear magnetic resonance (NMR) spectra were compared. **Figure S2** clearly reveals the distinctive peak position between the synthesized Li_2CS_3 @ Li_2S (208 ppm) and the CS_2 (192 ppm). Since the carbon atom becomes surrounded by a greater number of sulfur atoms in Li_2CS_3, the electron density on carbon decreased, and therefore, a downfield chemical shift was detected compared to that in CS_2. The color of the powder, FTIR spectra, and NMR obviously justify the formation of Li_2CS_3 on the synthesized compound surface.

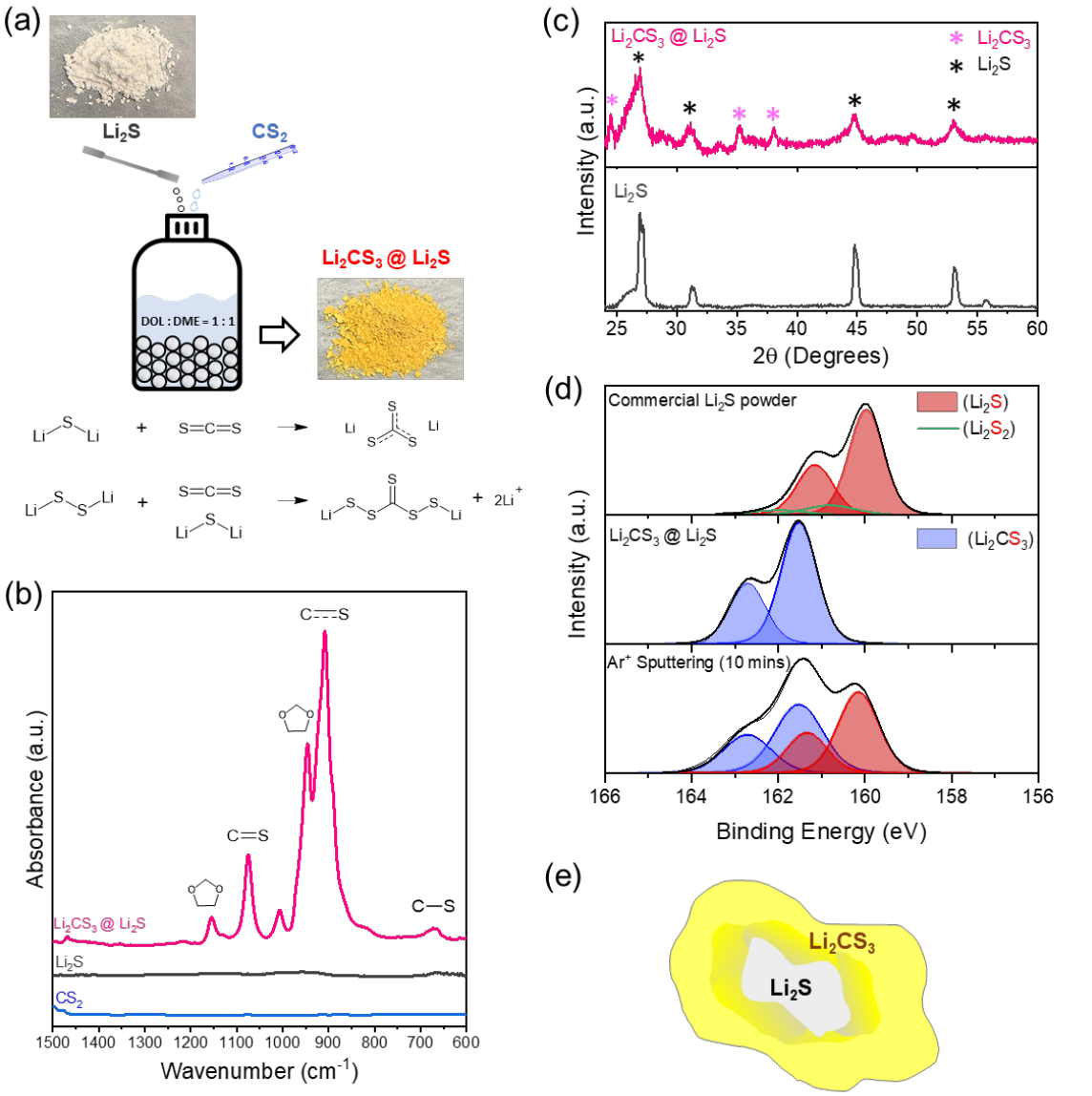

Figure 1. (a) Synthesis schematic and proposed reaction pathways for Li_2CS_3 @ Li_2S. (b) FTIR spectra of Li_2CS_3 @ Li_2S, Li_2S, and CS_2. (c) XRD patterns of Li_2CS_3 @ Li_2S and Li_2S. (d) S 2p XPS data of commercial Li_2S, Li_2CS_3 @ Li_2S, and Li_2CS_3 @ Li_2S after 10 mins of Ar^+ sputtering. (e) Proposed structure of the Li_2CS_3 @ Li_2S composite

To further investigate the crystalline structure of the obtained compound, X-ray diffraction (XRD) was performed (**Figure 1c**). The diffraction pattern of the synthesized compound reveals highly intense peaks for Li_2S, indicating that the conversion to Li_2CS_3 did not occur throughout the entire particle and the bulk still remained as Li_2S. The broadened

diffraction peaks of Li_2S reflect that Li_2S had lost crystallinity during the transformation reaction. Additional peaks located at $2\theta = 24°$, 35°, and 38° represent the existence of Li_2CS_3 at the surface of the particle. To confirm the surface chemistry and measure the thickness of the formed Li_2CS_3 layer, X-ray photoelectron spectroscopy (XPS) was conducted (**Figure 1d**). The S $2p_{3/2}$ peak observed at 161.5 eV corresponds to C ⎓ S on the surface of the Li_2CS_3 @ Li_2S composite, which is distinct from the sulfide (S^{2-}) peak known to be positioned at 160.5 eV.[34,35] The positive binding energy shift reveals a partial oxidation of sulfide (S^{2-}) while forming Li_2CS_3. It is important to note that distinct C = S and C – S bonds were not detected on the XPS, since the majority of the synthesized compound surface consisted of the C ⎓ S bond (Li_2CS_3). **Figure 1d** also shows the XPS measurements after an Ar^+ sputtering of the surface of Li_2CS_3 @ Li_2S. After sputtering for 10 mins, which corresponds to ~ 250 nm of material removal, the intensity of the C ⎓ S peak reduces, and the sulfide peak (160.5 eV) emerges. The XRD and XPS results signify that the reaction between Li_2S and CS_2 mainly occurred at the surface of the Li_2S particle, forming the Li_2CS_3, and the bulk remained as Li_2S (**Figure 1e**). Overall, the combination of characterization techniques confirmed the formation of Li_2CS_3-coated Li_2S (Li_2CS_3 @ Li_2S) via a wet ball milling synthesis.

With a firm understanding of Li_2CS_3 formation, anode-free full cells were assembled to evaluate the electrochemical performance. The discharged form of the cathode (Li_2CS_3 @ Li_2S) enables the implementation of an anode- free full cell configuration. With no excess Li existing in the system, the anode-free system can provide an accurate *in-situ* measurement of Li inventory loss rate at both the anode and cathode during cycling. The active materials were dissolved in a DOL / DME (1 : 1 vol.) media to drop cast between two carbon papers to ensure efficient electron transfer,[36] and construct in a form of Ni ‖ (Li_2CS_3 @ Li_2S) and Ni ‖ (Li_2S), as illustrated in **Figure S3**. The active material loading was 3 mg cm^{-2} and 75 µL of electrolyte was injected. All gravimetric capacities are reported with respect to the weight of the active material.

Figure 2a shows the second cycle galvanostatic charge-discharge curves of Ni ‖ (Li_2CS_3 @ Li_2S) and Ni ‖ (Li_2S) cells at C/5 rate. The Li_2S cathode displays a discharge capacity of 727 mA h g^{-1} at the end of its second cycle. As expected, the typical two voltage plateaus at 2.29 and 2.06 V are detected corresponding to the reduction of S_8 to higher order polysulfides (Li_2S_x, $4 \leq x \leq 8$) and further reduction of lower order polysulfides (Li_2S_x, $2 \leq x \leq 4$) to Li_2S, respectively. The capacity ratio between the first plateau and second plateau is 1 : 3, consistent with the number of electron transfer to sulfur at each reducing step. In sharp contrast, the Li_2CS_3 @ Li_2S cathode exhibit a slightly lower discharge capacity of 605 mA h g^{-1} at the end of its second cycle with a unique single discharge plateau contributing to the majority of the capacity (515 mA h g^{-1}). Surprisingly, the discharge plateau remarkably increased to an average voltage of 2.23 V. Even though the capacity is slightly lower than that of Li_2S cathode, the increased discharge voltage compensates, with the energy density of Li_2CS_3 @ Li_2S cathode comparable to that of Li_2S cathode. The main charge plateau of the Li_2CS_3 @ Li_2S cathode increased to 2.38 V (0.15 V polarization) whereas the Li_2S cathode is around 2.3 V (0.19 V polarization). It is clear to see that the potential difference between the charge and discharge curves is much smaller for the Li_2CS_3 @ Li_2S cell, suggesting an efficient reaction process with smaller energy barriers. Distinct charge-discharge curves for the Li_2CS_3 @ Li_2S cathode in comparison to the conventional Li_2S cathode are also evident in cyclic voltammetry (CV), as seen in **Figure 2b** and **Figure S4**. Certainly, such a noticeable difference in the voltage profile implies that the Li_2CS_3 causes the system to undergo a unique electrochemical process.

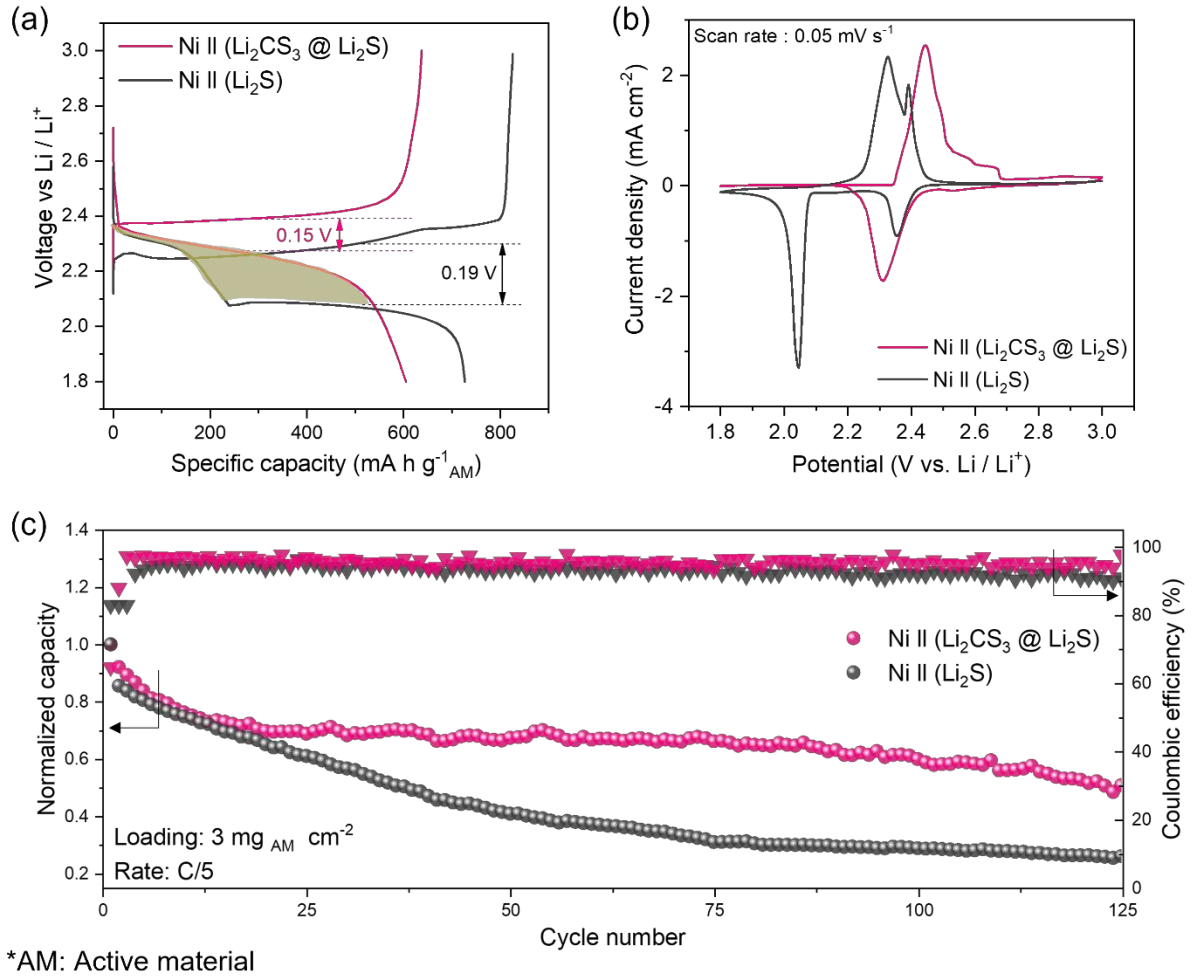

Figure 2. (a) 2nd cycle charge-discharge curves of full cells at C/5 rate, (b) cyclic voltammetry, and (c) normalized capacity and corresponding coulombic efficiency for Ni || (Li_2CS_3 @ Li_2S) and Ni || (Li_2S).

By confirming the different electrochemical processes taking place between the Li_2CS_3 @ Li_2S and Li_2S cathodes, the long-term cycling performance of Ni || (Li_2CS_3 @ Li_2S) and Ni || (Li_2S) were compared. In the initial cycling, the cells were charged up to 3.8 V and discharged down to 1.8 V at C/10 rate to overcome the activation barrier of Li_2S,[37] but the subsequent cycles were run at C/5 rate between 3.0 and 1.8 V. For the ease of comparison, capacities are normalized based on their initial discharge capacities and plotted. A significant improvement in the capacity retention is seen for the Li_2CS_3 @ Li_2S cathode. **Figure 2c** and

Figure S5 show that the Ni ‖ (Li_2CS_3 @ Li_2S) cell delivers good cyclic stability at the end of 125 cycles (330 mA h g^{-1}, 51 % retention), exhibiting a small capacity decay of 2.57 mA h g^{-1} per cycle with an average coulombic efficiency of 95.4 %. The capacity fade is rapid at the early stage (~ 20 cycles) and then becomes extremely stable until the 100th cycle. The Ni ‖ (Li_2S) cell, in contrast, exhibits poor cycling stability (220 mA h g^{-1}, 26 % retention) throughout 125 cycles with a fast capacity fade of 5.04 mA h g^{-1} per cycle. The average coulombic efficiency reaches only to 92.9 %. Similar to previous reports,[38] conventional anode-free cells with Li_2S exhibit consistent and drastic capacity fade throughout the entire cycle life.

To further evaluate the practicality of Li_2CS_3 in Li-S batteries, the cycling stability of anode-free cells were investigated at a high loading (6.6 mg cm^{-2}) and low electrolyte to sulfur ratio (E/S = 9 µL mg^{-1}) at C/10 rate. As shown in **Figure S6**, even with a high loading and low E/S ratio, the Li_2CS_3 @ Li_2S cathode outperforms (431 m Ah g^{-1}, 77 % retention) the conventional Li_2S cathode (366 m Ah g^{-1}, 60 % retention) at the end of 160 cycles. The average coulombic efficiency of Ni ‖ (Li_2CS_3 @ Li_2S) cell is 96.1 % whereas that of Ni ‖ (Li_2S) reaches only 95.4 %. It is noteworthy to emphasize that a major constituent towards the loss of electrochemical performance in anode-free full cells is attributed to the irreversible consumption of Li inventory in the system. The depletion of the active Li is mainly caused by the formation of "dead lithium," which is covered by (i) an insulating layer of Li_2S on the surface generated by the reduction of migrated polysulfides and (ii) compounds formed by the side reactions between the corrosive Li metal and the electrolyte. Thus, it is expected that the implementation of Li_2CS_3 as a cathode stabilizes Li-metal anode and prevents the loss of active Li. Moreover, the increased coulombic efficiency with the Li_2CS_3 @ Li_2S cathode indicates the suppression of polysulfide shuttling. Accordingly, the improved cycling

performance of the Li_2CS_3-containing anode-free cell is a result of the combination of stabilized Li-metal anode and suppression of polysulfide shuttling.

To isolate the effect of Li_2CS_3 on the Li-metal anode side and to focus on the cathode, Li ‖ (Li_2CS_3 @ Li_2S) and Li ‖ (Li_2S) half cells were assembled. In the half-cell configuration where a large excess of Li exists, the deactivation of Li inventory upon cycling can be recovered. Hence, the electrochemical performance of the half cell predominantly depends on the cathode. Similar to the anode- free cell, the Li_2CS_3 @ Li_2S cathode shows improved cyclic stability at the end of 180 cycles (603 m Ah g^{-1}, 96% retention from peak capacity) compared to Li_2S cathode (317 m Ah g^{-1}, 53% retention from peak capacity) (**Figure S7**). The voltage profile of Li_2CS_3 @ Li_2S cathode is analogous to the anode-free cell, which had a dominant plateau around 2.3 V (**Figure S8**). The distinctive voltage profile again confirms the unique electrochemical reaction of Li_2CS_3. Interestingly, a lower-voltage plateau is detected at 2.05 V for the Li ‖ (Li_2CS_3 @ Li_2S) cell, contributing to a small amount of the overall capacity (35 mA h g^{-1}). This indicates that while Li_2CS_3 is going through the redox reaction that generates majority of the capacity, a small portion of the Li_2S is active and behaves like the conventional Li-S cell. Assuming a complete replenishment of Li loss upon cycling in the Li-excess half cell, the superior cycling performance of Li ‖ (Li_2CS_3 @ Li_2S) compared to the Li ‖ (Li_2S) cell reveals that Li_2CS_3 is contributing to the improvement in the cathode and dramatically reduce the polysulfide shuttle effect. By confirming the prolonged cycle life in virtue of the Li_2CS_3 implementation both in the anode-free cells and half cells, it is necessary to examine how Li_2CS_3 is impacting the cathode and anode to result in such a performance enhancement.

To investigate the origin of the change in the reaction process and understand the effect of Li_2CS_3 on cathode, FTIR spectroscopy was conducted on the cathode surface after the initial charge. **Figure S9** shows the presence of C = S, C – S, and C⁼⁼S bonds, which were not

detected with the Li_2S cathode. The absorbance corresponding to the C = S bond dramatically increased whereas a relative decrement is seen corresponding to the C ⎓ S bond. The result signifies the transformation of trithiocarbonate to a new structure containing C = S bond. This is further supported by the XPS data in **Figure 3a**. After charging the cell, the S $2p_{3/2}$ peak at 163.14 eV emerges, which confirms the formation of C = S bond.[39] The bridging sulfur peak at 164 eV was also detected with weak intensity. Based on the XPS and FTIR analysis, it is expected that delithiated Li_2CS_3 may get connected by the bridging sulfur, forming the [– CS_3 – S_x – CS_3 –] oligomer structure during the charging process. **Figure S10** reveals a uniform coverage by a [– CS_3 – S_x – CS_3 –] layer on the charged cathode surface. In order to evaluate the thickness of the oligomer layer, the cathode surface was sputtered for 10 mins. Even after sputtering, the noticeable intensities of the C = S bond and bridging sulfur signal imply the existence of an oligomer structure to a depth of 250 nm from the surface. The relative increase in the intensity of the C ⎓ S bond suggest that the bottom of the cathode is not fully delithiated and remains as Li_2CS_3. As expected, a discernable peak of Li_2S at 160.2 eV was observed after Ar^+ sputtering, which confirms that the synthesized compound surface is coated with Li_2CS_3, and the interior remained as Li_2S. Thus, the charged cathode electrode forms a unique layered composition, as illustrated in **Figure 3b**.

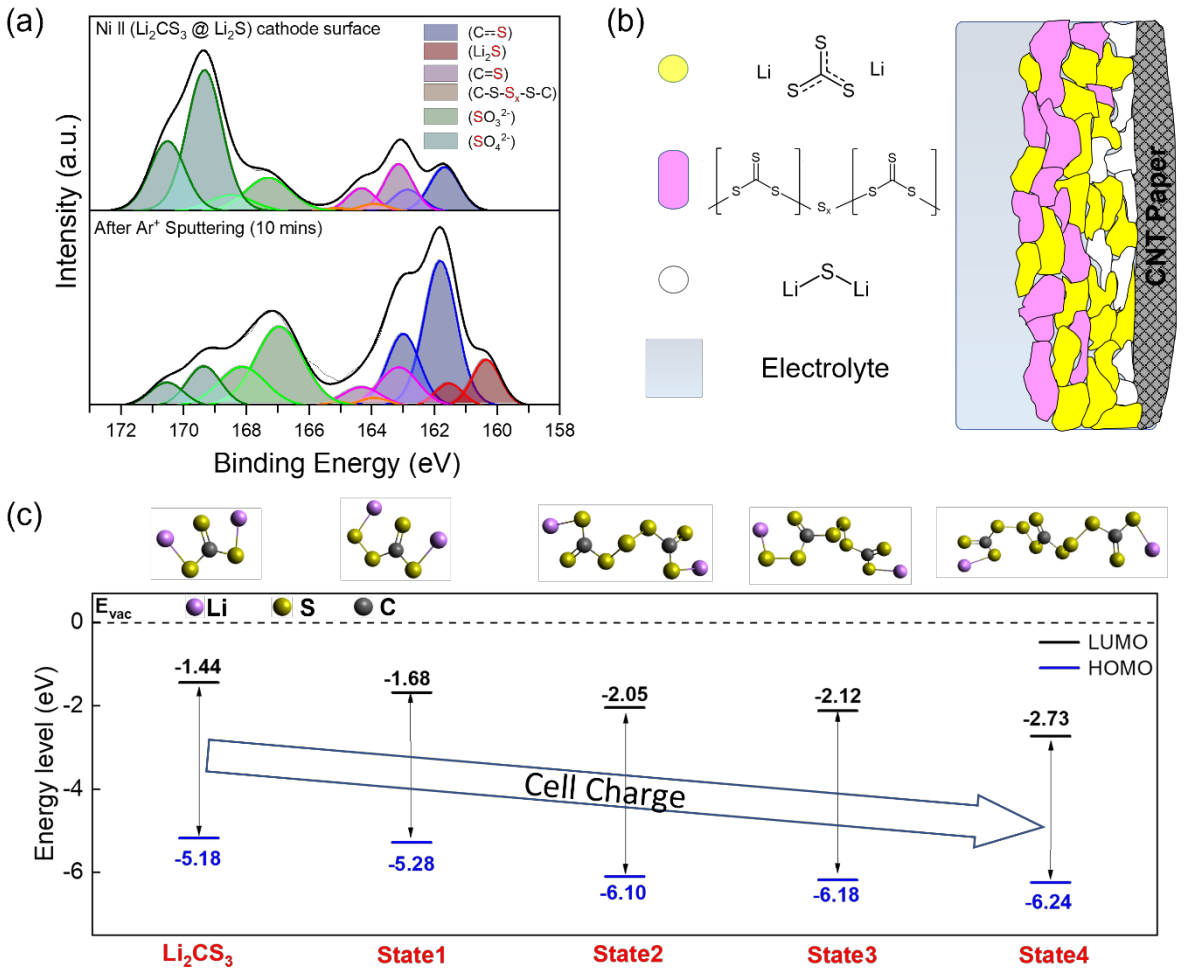

Figure 3. (a) XPS spectra before and after Ar^+ sputtering and (b) schematic illustration of the charged Li_2CS_3 @ Li_2S electrode. (c) LUMO / HOMO energy levels at different states upon cell charge. The state numbers correlate to those in Scheme 1.

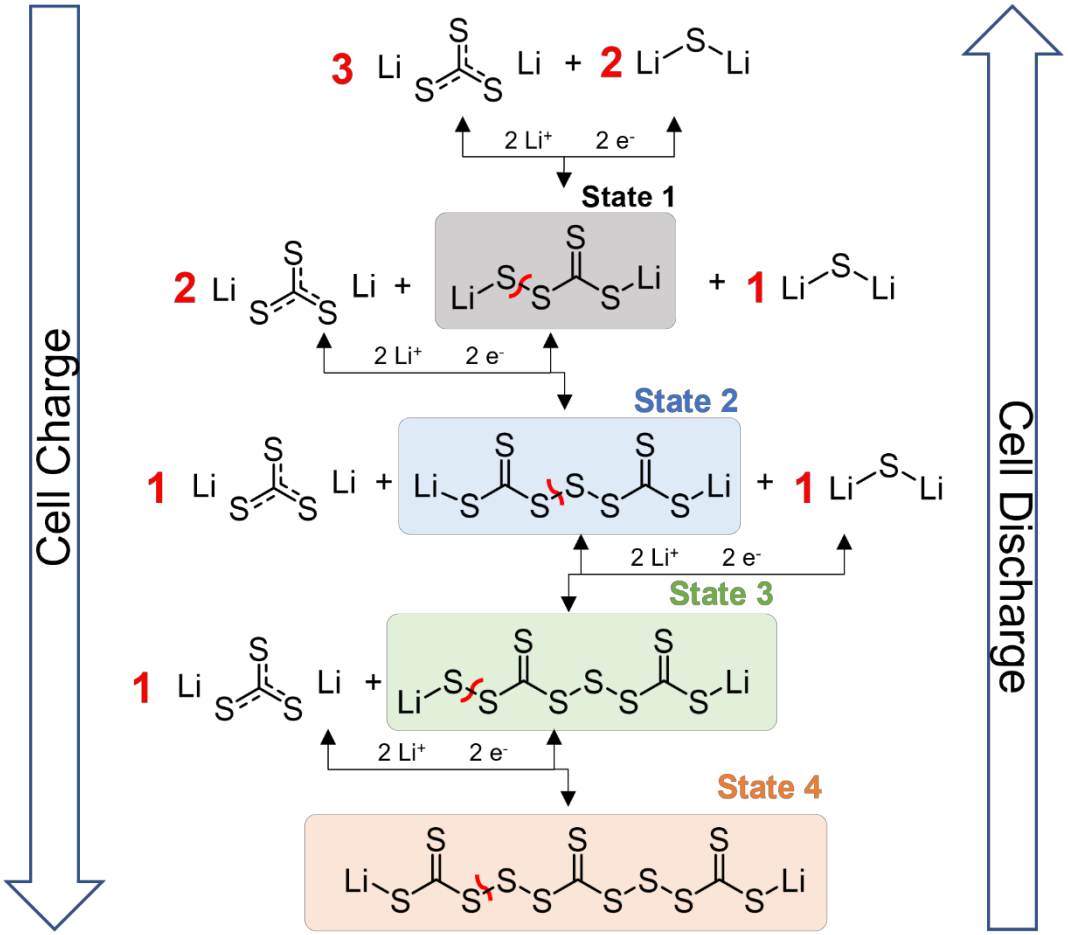

Scheme 1. States of the chemical reaction of Li_2CS_3 @ Li_2S to [– CS_3 – S_x – CS_3 –].

Based on the observations from the cathode characterization, the states from the Li_2CS_3 @ Li_2S cathode to the expected state of the final charged oligomer structure are outlined in **Scheme 1**. In order to further understand the energetics of the reaction and verify the feasibility of the reaction taking place, first-principle DFT calculation was performed. **Figure 3c** shows the lowest unoccupied molecular orbital (LUMO) and highest occupied molecular orbital (HOMO) energy levels of each state upon cell charge. The state numbers in the plot correspond to the numbers in **Scheme 1**. The gradually decreasing trend of LUMO and HOMO energy levels during cell charge supports that the reaction mechanism is energetically plausible. For the sake of illustration purposes, a ratio of Li_2CS_3 : Li_2S = 3 : 2 is considered in the scheme. As Li_2CS_3 @ Li_2S (HOMO: -5.18 eV) loses two electrons and two Li-ions, the molecular structure of **State 1** (HOMO: -5.28 eV) is formed. The small energy gap between

Li_2CS_3 and **State 1** indicates that those two states co-exist at the early stage of charge. The subsequent reaction is accompanied by a reaction between Li_2CS_3 and **State 1** to form an oligomer structure of **State 2** (HOMO: -6.10 eV). The sudden jump of HOMO / LUMO level between **State 1** and **State 2** potentially indicates that other intermediate structures could exist, which are not considered in here. The consecutive electron-transfer process causes the reaction between **State 2** and Li_2S, resulting in the formation of **State 3** (HOMO: -6.18 eV). Finally, the reaction between Li_2CS_3 and **State 3** leads to the formation of a long-chained oligomer structure of **State 4** (HOMO: -6.24 eV). Likewise, the small energy gap between **State 2, State 3,** and **State 4** implies the concurrency of the three structures, presumably at the later stage of charge. If the starting ratio of Li_2CS_3 : Li_2S changes with more Li_2S, the final charged oligomer structure will contain more of the polysulfide form. It is important to note that the HOMO / LUMO cannot directly signify the redox energies since they are derived from approximated electronic structure theory of isolated molecules, which neglects the concentration ratio of active redox species. However, it still implies that each proposed state of molecules is physically plausible, and the oxidation process (charging) is decreasing the HOMO / LUMO level, which makes each progressive state more reductive. The suggested mechanism can alter the reaction pathway of sulfur and reveals the unique discharge voltage profile, which is distinctive from the conventional reaction process of sulfur.

It is important to investigate how the oligomer layer formed on the cathode surface enhances the cyclic performance of the cell. In conventional Li-S batteries, polysulfides facilitate a solution-mediated redox and improve the utilization of active materials. However, the migration of polysulfides from the cathode to the anode causes irreversible parasitic reactions that deteriorate the capacity during cycling. Moreover, as higher-order polysulfide chains reduce to lower-order polysulfides (Li_2S / Li_2S_2), they precipitate out of the electrolyte due to low solubility in most electrolytes. It is also well known that conventional Li-S batteries experience rapid capacity fade due to the passivation of an insulating Li_2S / Li_2S_2 on

the cathode surface.[40,41] These poorly-conducting layers block the available area of conducting carbon and hinder ion and electron transport.

In contrast, the Li_2CS_3 @ Li_2S cathode suppresses the generation of polysulfides and instead forms the intermediates, as discussed in **Scheme 1**. The oligomer-structured [– CS_3 – S_x – CS_3 –] has heavier mass and stronger attachment to the carbon frame compared to the polysulfides, which prohibits the shuttle effect. To verify the effect of polysulfide suppression, half cells after 30 cycles were disassembled. **Figure S11** clearly shows the less yellow-colored separator from the Li ‖ (Li_2CS_3 @ Li_2S) cell, which corresponds to less polysulfide generation and shuttling compared to the control cell. Furthermore, these intermediate structures may become passivated on the cathode surface and form a highly conductive layer by virtue of the covalent character between carbon and sulfur atoms. The similar electronegativity between S (2.58) and C (2.55) atoms delocalize electrons, which contributes to the improved electronic conductivity. The conductive layer on the cathode surface provides sufficient ionic / electronic pathways and maintains the utilization of active materials over cycling. The analysis on the cathode coupled with the DFT strongly supports the conclusion that the insertion of Li_2CS_3 in the system not only suppresses polysulfide generation and shuttling, but also forms a conductive layer on the cathode surface and contributes to the extended cycle life.

Verifying the effect of Li_2CS_3 on the cathode, the remaining question is the influence of the presence of Li_2CS_3 in the system can have on Li-metal anode. Scanning electron microscopy (SEM) images of the anode after 30 cycles reveal prominent differences in the surface morphology of the deposited Li. As shown in **Figure 4a**, conventional Ni ‖ (Li_2S) cell shows a mossy and filamentous morphology of Li. In contrast, **Figure 4b** and **Figure S12** confirm that the Ni ‖ (Li_2CS_3 @ Li_2S) cell supports the formation of a smooth, planar, dense Li surface. It is well known that the uniform morphology of Li with a low-surface area can

minimize the parasitic side reactions with the electrolyte and polysulfides, significantly reducing the depletion of active Li in the system. The contrasting Li morphology is in good agreement with the superior cyclic stability and higher coulombic efficiency of the Ni ‖ (Li_2CS_3 @ Li_2S) anode-free cell.

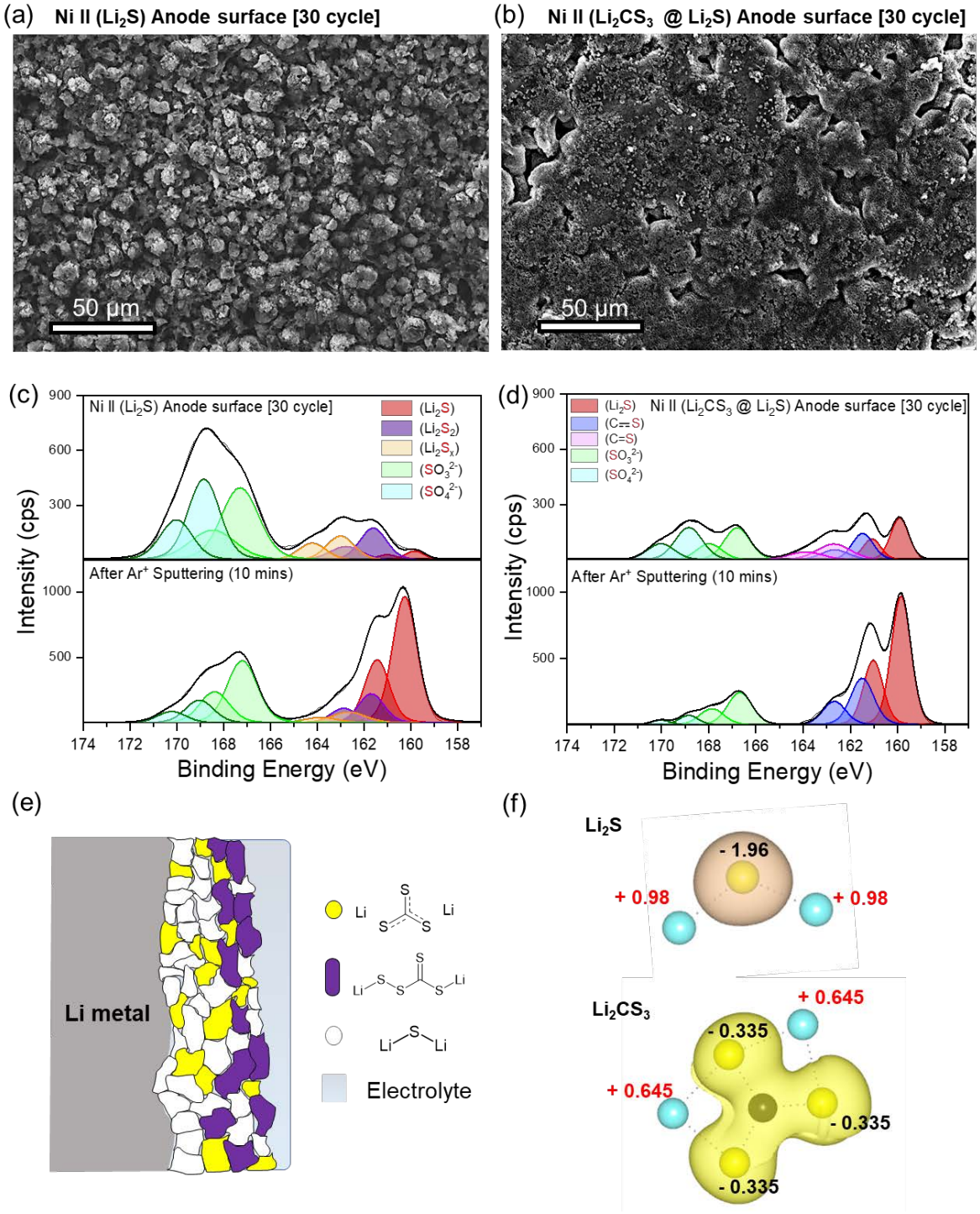

Figure 4. SEM image of the anodes after 30 cycles: (a) Ni ‖ (Li_2S) and (b) Ni ‖ (Li_2CS_3 @ Li_2S). XPS data before and after Ar^+ sputtering of the anodes after

30 cycles: (c) Ni ‖ (Li_2S) and (d) Ni ‖ (Li_2CS_3 @ Li_2S). (e) SEI layer schematic of Ni ‖ (Li_2CS_3 @ Li_2S). (f) Bader charge analysis of Li_2S and Li_2CS_3.

To further explain the source of the improved Li plating and stripping behavior, the chemical compositions of the 30-cycled anode SEI layer were analyzed with XPS. As shown in **Figure 4c**, the S 2p spectra is dominated by the oxidized sulfur species (SO_3^{2-} at 167.2 eV and SO_4^{2-} at 168.9 eV) from LiTFSI salt decomposition in the Ni ‖ (Li_2S) anode. A small intensity of reduced sulfur species is present as a minor component. After sputtering the surface for 10 mins to remove the salt decomposition layer, discernable reduced sulfur signals were detected. The result is in good agreement with the previous report,[42] explaining that due to the high-surface area mossy growth of Li causing parasitic reactions, excess amount of byproducts from the reaction between Li and electrolyte cover the Li-metal surface during cycling. This irreversible reaction between the Li and the electrolyte creates "dead lithium" and, leading to the loss of active Li inventory. In sharp contrast, **Figure 4d** shows that Ni ‖ (Li_2CS_3 @ Li_2S) anode displays the S 2p spectrum with a much less intensity of oxidized sulfur species and relatively high reduced sulfur species. The peak corresponding to C $\equiv$ S (161.5 eV) and C = S (162.9 eV) were also detected on the surface of Li. The existence of carbon-sulfur bonds is confirmed by FTIR, as shown in **Figure S13**. The quantification of the spectra reveals that the oligomer-structured carbon-sulfur species from cathode transferred to the anode and partially reduced to Li_2S, Li_2CS_3, and Li_2CS_4 upon cycling. The presence of partially reduced Li_2CS_4 is expected at the surface of Li due to the hindered metallic Li and electron conduction pathways. To evaluate the thickness of carbon-sulfur species containing the SEI layer, Ar^+ sputtering for 10 mins was conducted. Interestingly, C = S bond attenuated and only the peaks corresponding to C $\equiv$ S and Li_2S remained. This reveals that in the vicinity of the deposited Li, kinetic hinderance of metallic Li and electrons are minimized, and the strongly reducing nature of Li leads to a complete reduction of Li_2CS_4 into Li_2S and Li_2CS_3.

Thus, the introduction of Li_2CS_3 alters the chemical composition of the Li-electrolyte interphase to a high amount of reduced sulfur species (Li_2S, Li_2CS_3) and a less amount of oxidized sulfur species (SO_3^{2-}, SO_4^{2-}). The schematic of the SEI layer formed by Li_2CS_3 is outlined in **Figure 4e**.

Answering the question as to why the inclusion of Li_2CS_3 in the SEI improves Li plating/stripping behavior requires an analysis of the properties of the SEI components. The intrinsic electron density spread on Li_2S and Li_2CS_3 was calculated via the Bader charge analysis. **Figure S14** illustrates the relaxed structure of each molecule. The relaxed structure of Li_2S shows similar bond length and angle as in the literature,[43] which supports the validity of the calculation, and an equivalent method was applied for Li_2CS_3. As shown in **Figure 4f**, the binary sulfide (Li_2S), which is the main component of SEI formed in anode-free Ni ‖ (Li_2S) cells, has a highly ionic bond due to the large electronegativity difference between Li (0.98) and S (2.58). The sulfur atom in Li_2S possesses high electron density, resulting in a net charge of -1.96. In this case, the highly negatively charged sulfur atoms will produce a large diffusion barrier against Li^+ ions and engender an inhomogeneous Li deposition. In contrast, the more covalent characteristics of the ternary sulfide (Li_2CS_3) spreads the electron density between the carbon and the surrounding sulfur atoms, which leads to an average net charge of only -0.335 on sulfur. In this case, the reduced charge on sulfur alleviates the diffusion barrier for Li^+ ions and facilitates a uniform Li-ion flux. This contributes to an improved Li plating and stripping behavior. As a result, the stable Li_2CS_3-containing SEI layer on the anode surface facilitates the deposition of a dense, low-surface area Li, minimizing the sites that can react with the electrolyte and polysulfides. This considerably helps sustain the Li inventory in the system, leading to enhanced cycling stability and higher coulombic efficiency.

3. Conclusion

To conclude, for the first time, we utilized Li_2CS_3-coated Li_2S as a cathode and successfully enhanced the electrochemical performance. The Li_2CS_3 @ Li_2S cathode was synthesized by a facile wet-ball milling process. Benefiting from a unique reaction mechanism, the average discharge voltage increased to 2.23 V for the Li_2CS_3 @ Li_2S cathode compared to 2.11V for the Li_2S cathode. Furthermore, Li_2CS_3 acts as a dual-functional material to improve the cathode by forming an oligomer-structured layer on the surface to reduce polysulfide shuttling and provide electronic/ionic pathway to the active material. It also enhances the performance of the anode by forming a robust protective layer that contributes to homogeneous Li plating and stripping. As a result, the Li_2CS_3 @ Li_2S cathode displays superior cycle life in both half-cells and anode-free full-cells compared to the Li_2S cathode. The results with the Li_2CS_3 @ Li_2S composite as the active material provide good insights and opportunities to design an efficient and practical Li–S system by simultaneously stabilizing both the anode and cathode.

Supporting Information

Supporting Information is available from the Wiley Online Library or from the author.

Acknowledgements

This work was supported by the National Science Foundation, Division of Chemical, Bioengineering, Environmental, and Transport Systems, under award number 2011415.

Received: ((will be filled in by the editorial staff))
Revised: ((will be filled in by the editorial staff))
Published online: ((will be filled in by the editorial staff))

References

[1] A. Manthiram, *Nat Commun.* **2020**, *11*, 1550.

[2] A. Manthiram, *ACS Cent. Sci.* **2017**, *3*, 1063.

[3] A. Manthiram, S.-H. Chung, C. Zu, *Adv. Mater.* **2015**, *27*, 1980.

[4] S.-H. Chung, A. Manthiram, *Adv. Mater.* **2019**, *31*, 1901125.

[5] A. Manthiram, Y. Fu, S.-H. Chung, C. Zu, Y.-S. Su, *Chem. Rev.* **2014**, *114*, 11751.

[6] J. Wang, J. Yang, C. Wan, K. Du, J. Xie, N. Xu, *Adv. Funct. Mater.* **2003**, *13*, 487.

[7] B. Zhang, X. Qin, G. R. Li, X. P. Gao, *Energy Environ. Sci.* **2010**, *3*, 1531.

[8] Z. G, Y. Y, C. Jj, H. Ss, C. Y, *Nano Lett.* **2011**, *11*.

[9] J. Guo, Y. Xu, C. Wang, *Nano Lett.* **2011**, *11*, 4288.

[10] J. He, Y. Chen, A. Manthiram, *Adv. Energy Mater.* **2019**, *9*, 1900584.

[11] A. Bhargav, Y. Ma, K. Shashikala, Y. Cui, Y. Losovyj, Y. Fu, *J. Mater. Chem. A.* **2017**, *5*, 25005.

[12] A. Bhargav, S. V. Patil, Y. Fu, *Sustainable Energy Fuels* **2017**, *1*, 1007.

[13] Z. Shadike, S. Tan, Q.-C. Wang, R. Lin, E. Hu, D. Qu, X.-Q. Yang, *Mater. Horiz.* **2021**, *8*, 471.

[14] X. Yu, A. Manthiram, *Energy Environ. Sci.* **2018**, *11*, 527.

[15] M. Wild, L. O'Neill, T. Zhang, R. Purkayastha, G. Minton, M. Marinescu, G. J. Offer, *Energy Environ. Sci.* **2015**, *8*, 3477.

[16] S. S. Zhang, *J. Power Sources* **2013**, *231*, 153.

[17] J. Heine, S. Krüger, C. Hartnig, U. Wietelmann, M. Winter, P. Bieker, *Adv. Energy Mater.* **2014**, *4*, 1300815.

[18] Y. X. Ren, L. Zeng, H. R. Jiang, W. Q. Ruan, Q. Chen, T. S. Zhao, *Nat Commun.* **2019**, *10*, 3249.

[19] J. Park, J. Jeong, Y. Lee, M. Oh, M.-H. Ryou, Y. M. Lee, *Adv. Mater. Interfaces.* **2016**, *3*, 1600140.

[20] S. Nanda, A. Bhargav, A. Manthiram, *Joule* **2020**, *4*, 1121.

[21] Q. Pang, X. Liang, A. Shyamsunder, L. F. Nazar, *Joule* **2017**, *1*, 871.

[22] H. Shin, M. Baek, A. Gupta, K. Char, A. Manthiram, J. W. Choi, *Adv. Energy Mater.* **2020**, *10,* 2001456.

[23] W. Guo, W. Zhang, Y. Si, D. Wang, Y. Fu, A. Manthiram, *Nat Commun.* **2021**, *12*, 3031.

[24] S. Gu, Z. Wen, R. Qian, J. Jin, Q. Wang, M. Wu, S. Zhuo, *ACS Appl. Mater. Interfaces* **2016**, *8*, 34379.

[25] Y. Ein-Eli, *J. Electroanal. Chem.* **2002**, *531*, 95.

[26] Y. Chu, X. Cui, Q. Pan, *ACS Appl. Energy Mater.* **2018**.

[27] H. Seidel, R. Meyn, *Zeitschrift für Naturforschung B* **1971**, *26*, 1192.

[28] J. Coates, In *Encyclopedia of Analytical Chemistry*, **2006**.

[29] J. D. Magdaline, T. Chithambarathanu, *Vibrational Spectra (FTIR , FT-Raman), NBO and HOMO , LUMO Studies of 2-Thiophene Carboxylic Acid Based On Density Functional Method*, **2015**.

[30] J. S. Kwiatkowski, J. Leszczyński, I. Teca, *Journal of Molecular Struct.* **1997**, *436–437*, 451.

[31] D. M. Wiles, B. A. Gingras, T. Suprunchuk, *Canadian Journal of Chem.* **2011**.

[32] C. N. R. Rao, R. Venkataraghavan, *Spectrochimica Acta* **1962**, *18*, 541.

[33] P. Cao, J. Yao, B. Ren, R. Gu, Z. Tian, *J. Phys. Chem. B* **2002**, *106*, 10150.

[34] D. Foix, D. Gonbeau, G. Taillades, A. Pradel, M. Ribes, *Solid State Sci.* **2001**, *3*, 235.

[35] M. Helen, M. A. Reddy, T. Diemant, U. Golla-Schindler, R. J. Behm, U. Kaiser, M. Fichtner, *Sci Rep* **2015**, *5*, 12146.

[36] Y. Fu, Y.-S. Su, A. Manthiram, *Adv. Energy Mater*. **2014**, *4*, 1300655.

[37] Y. Yang, G. Zheng, S. Misra, J. Nelson, M. F. Toney, Y. Cui, *J. Am. Chem. Soc.* **2012**, *134*, 15387.

[38] S. Nanda, A. Manthiram, *Energy Environ. Sci.* **2020**, *13*, 2501.

[39] A. Bhargav, A. Manthiram, *Adv. Energy Mater.* **2020**, *10*, 2001658

[40] R. Demir-Cakan, *J. Power Sources* **2015**, *282*, 437.

[41] M. Cuisinier, P.-E. Cabelguen, S. Evers, G. He, M. Kolbeck, A. Garsuch, T. Bolin, M. Balasubramanian, L. F. Nazar, *J. Phys.Chem. Lett.* **2013**, *4*, 3227

[42] S. Nanda, A. Gupta, A. Manthiram, *Adv. Energy Mater.* **2018**, *8*, 1801556.

[43] H. Park, D. J. Siegel, *Meet. Abstr.* **2018**, *MA2018-01*, 304.

Supporting Information

Lithium trithiocarbonate as a dual-function electrode material for high-performance lithium-sulfur batteries

*Hyunki Sul, Amruth Bhargav, and Arumugam Manthiram**

Experimental Section

Preparation of Li_2CS_3 @ Li_2S and Li_2S cathode

Lithium trithiocarbonate (Li_2CS_3) coated lithium sulfide (Li_2S) cathode were obtained by a typical wet-ball milling method. Commercial Li_2S (99.9% metals basis, Sigma Aldrich) was processed with a planetary ball milling system (Fritsch Pulverisette 6) for 12 h (at intervals of 30 min milling followed by 30 min resting) at 400 rpm. Refined Li_2S powder was transferred to a PTFE bottle inside an argon-filled glovebox, and carbon disulfide (CS_2, Alfa Aesar) was added in a 1 : 3 mole ratio. 30 mL of 1,3-dioxolane (DOL, Sigma Aldrich) and 1,2-dimethoxyethane (DME, Sigma Aldrich) in a volume ratio = 1 : 1 were added as a dispersing medium and yttria-stabilized zirconia (YSZ) grinding balls were used to create a homogenous slurry. The bottle was processed for 48 h with a roll jar milling system (US Stoneware 802 CVM). The resultant slurry was dried under vacuum to remove the solvent and excess amount of CS_2. The Li_2CS_3 @ Li_2S powder obtained was mixed with commercial multi-walled carbon nanotubes (MWCNT, Sigma Aldrich) in a 7 : 3 weight ratio with 30 mL of DOL / DME co-solvents for 48 h. The homogeneous Li_2CS_3 @ Li_2S slurry was drop casted between two pieces of carbon paper (AvCarb P50, 7/16-inch diameter) and dried inside a glove box to obtain the Li_2CS_3 @ Li_2S composite cathode with an active material loading of 3 mg cm^{-2}. Li_2S cathodes were prepared by a similar procedure. The refined Li_2S powder was combined with commercial MWCNT in a 7 : 3 weight ratio. 30 mL of DOL / DME co-solvents and YSZ

grinding balls were added to a PTFE bottle. The bottle was further processed by a roll jar milling system for 48 h to form a uniform slurry and then drop casted between two pieces of carbon paper to create a cathode with a final Li_2S loading of 3 mg cm^{-2}. Li_2S and CS_2 were handled inside an argon-filled glovebox or in sealed ball-milling containers throughout the entire process.

Material characterization

The wet-ball milled slurry was drop casted and dried inside a glass vial at 50°C for 2 h to remove the solvent, and the powder was collected for characterization. X-ray diffraction (XRD) was performed with a Rigaku MiniFlex 600 X-ray diffractometer, equipped with Cu K radiation. Fourier transform infrared spectra (FTIR) were recorded with a Thermo Scientific-Nicolet iS5 FTIR spectrometer. Samples for nuclear magnetic resonance (NMR) spectroscopy were prepared inside an argon-filled glovebox consisting of 0.1 g of the powder in D_6-Acetone. ^{13}C-NMR spectroscopy was performed with a Bruker Avance III 500 MHz NMR spectrometer. 1092 scans were performed for each sample, and the chemical shifts were calibrated with the residual solvent peak as an internal standard. X-ray photoelectron spectroscopy (XPS) data were collected with a Kratos Analytical spectrometer. The spectra were obtained with a monochromatic Al Kα source (1468.5 eV) at 12 kV and 10 mA. Sputtering of the samples was conducted by exposing the surface to an Ar^+ ion beam for 10 mins from an equipped Ar gas ion gun source. The obtained binding energies were calibrated based on the hydrocarbon C 1s peak at 284.8 eV. All the peak fittings and data processing were carried out with the CasaXPS software. The morphology study was performed with a FEI Quanta 650 scanning electron microscopy (SEM). Charged and discharged electrodes for SEM, XPS, and FTIR measurements were rinsed with 30 μL DME, followed by drying to eliminate the residual soluble salts and solvents.

Cell assembly and electrochemical performance measurements

All cells were assembled inside an argon-filled glovebox with CR2032 coin cells. The free-standing cathode was prepared by drop casting the slurry to carbon papers as described earlier. Anode-free Ni || (Li_2CS_3 @ Li_2S) and Ni || (Li_2S) full cells were assembled with, respectively, the Li_2CS_3 @ Li_2S composite cathode and Li_2S cathode combined with 9/16-inch diameter Ni foil (MTI Corporation) as the host-less anode. 3/4-inch diameter Celgard 2325 separator was used. The standard electrolyte consisted of 1 M LiTFSI / 0.2 M $LiNO_3$ in DOL : DME (volume ratio = 1 : 1). Similarly, Li || (Li_2CS_3 @ Li_2S) and Li || (Li_2S) half cells were assembled with lithium metal foil as an anode. The assembled cells were rested for 12 h at ambient temperature prior to the testing. Cells were initially charged at C/10 rate until the voltage reached 3.8 V, followed by galvanostatic discharging at 1.8 V. The subsequent cycles were charged and discharged at C/5 rate between 3.0 and 1.8 V. All cell cycling data were obtained with an Arbin battery testing system. Cyclic voltammetry (CV) was conducted on a Biologic VMP potentiostat in the voltage range of 3.0 to 1.8 V at a rate of 0.05 mV s^{-1}.

High loading and lean electrolyte test

The electrode for the high loading and lean electrolyte cells was prepared by drop casting 6.6 mg cm^{-2} of active materials in between two pieces of carbon papers. 30 μL of electrolyte was added to the cathode and an additional 30 μL electrolyte was used to infiltrate the separator and Ni foil. The E/S ratio was controlled to be 9 μL per mg of active material.

Computational methods

Texas Advanced Computing Center (TACC) was used as a computational resource for running all the calculations. The calculations were carried out with *Vienna ab-initio* Simulation Package (VASP) and Gaussian 16 Rev. A.03. The molecular structure input files were prepared with Avogadro 1.2.0. To calculate the HOMO/LUMO energy, the structure

files were converted to .XYZ format with VESTA 3.5.7, and initially relaxed with VASP. A conjugate-gradient algorithm was used for ionic relaxation until the total free energy difference is smaller than 5×10^{-5} eV / atom. The relaxed ionic structure was subsequently optimized with Gaussian. The hybrid B3LYP 6-311 +G(d,p) method was used to optimize the structure, and the solvent was implicitly modeled using THF, which has similar properties to DOL/DME. To calculate the average net charge of sulfur atoms, Bader charge analysis was performed with the F90 open source code (URL: https://theory.cm.utexas.edu/henkelman/code/bader/).

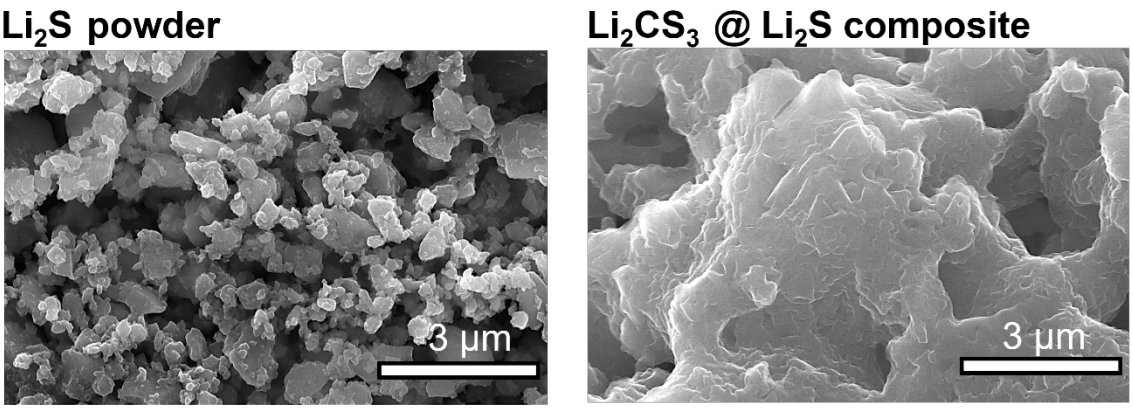

Figure S1. SEM images of Li_2S and Li_2CS_3 @ Li_2S powder.

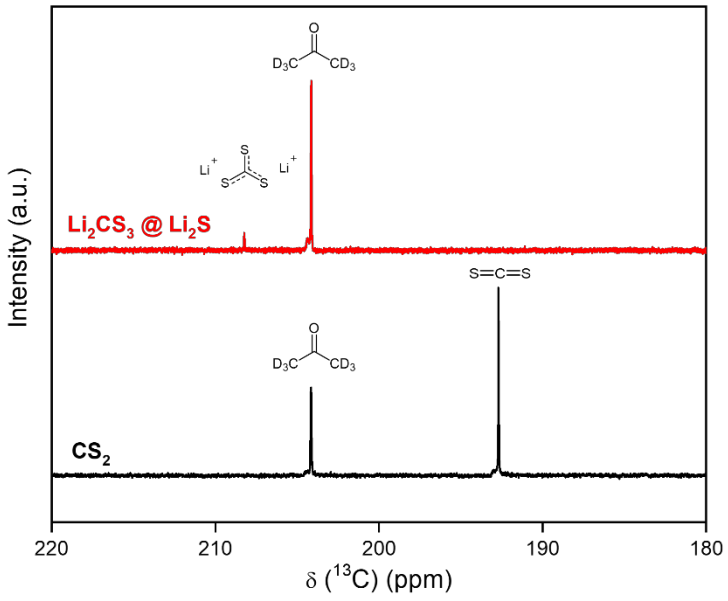

Figure S2. ^{13}C NMR spectra of Li_2CS_3 @ Li_2S and CS_2.

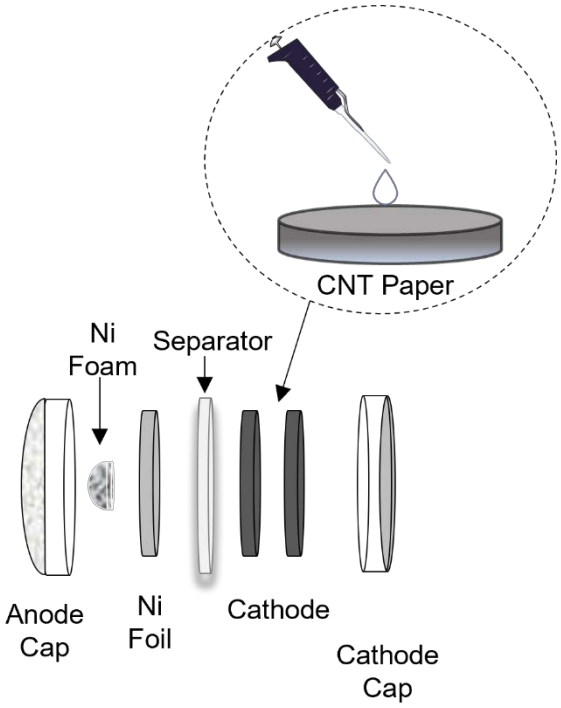

Figure S3. Schematic of the anode-free full cell assembly.

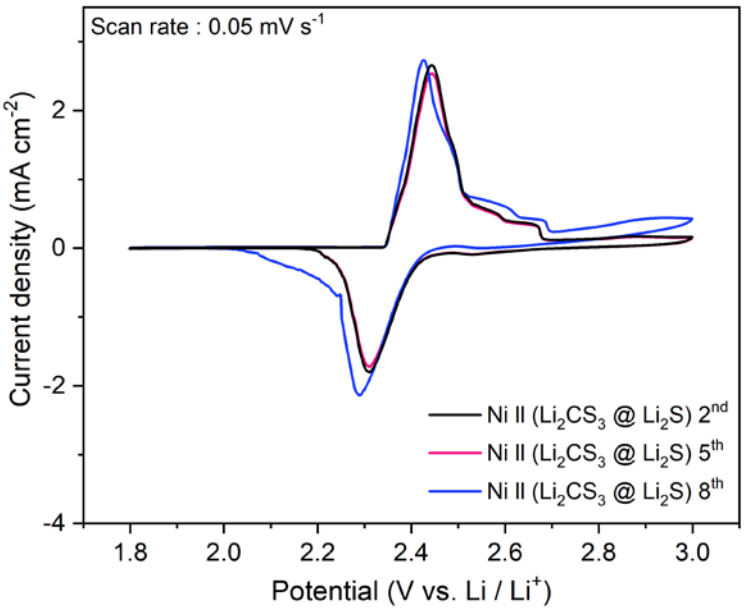

Figure S4. Cyclic voltammetry curve of Ni || (Li_2CS_3 @ Li_2S) at 2^{nd} , 5^{th} , and 8^{th} cycles.

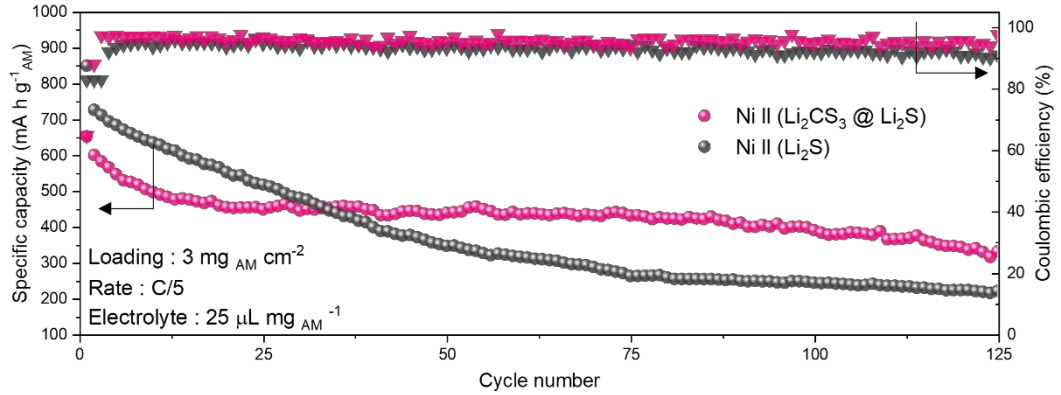

Figure S5. Long-term cycle life and corresponding coulombic efficiency for Ni || (Li_2CS_3 @ Li_2S) and Ni || (Li_2S) full cells at C/5 rate.

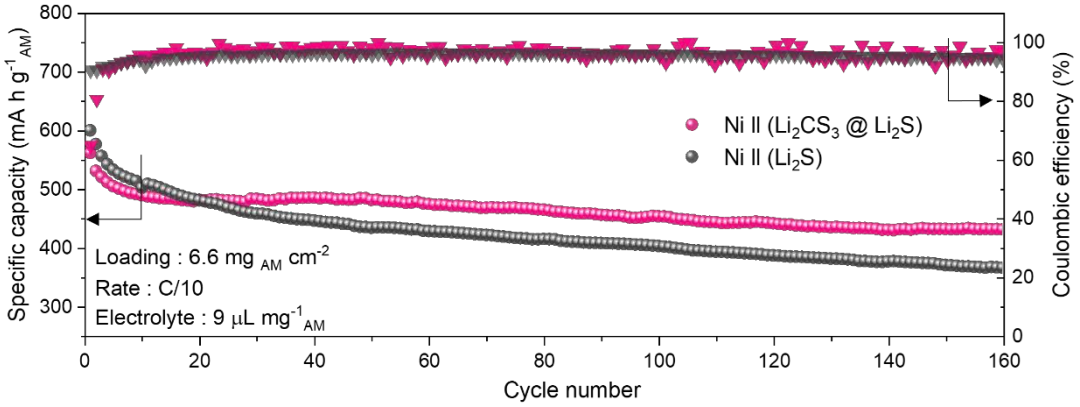

Figure S6. Long-term cycle life and corresponding coulombic efficiency for Ni || (Li_2CS_3 @ Li_2S) and Ni || (Li_2S) full cells at high loading (6.6 mg cm^{-2}) and low E/S ratio (9 µL mg^{-1}) at C/10 rate.

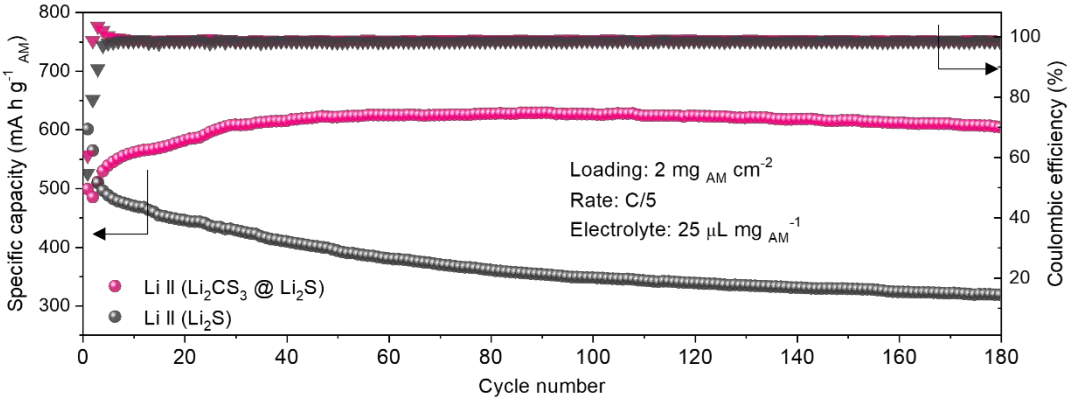

Figure S7. Long-term cycle life and corresponding coulombic efficiency for Li || (Li_2CS_3 @ Li_2S) and Li || (Li_2S) half cells at C/5 rate.

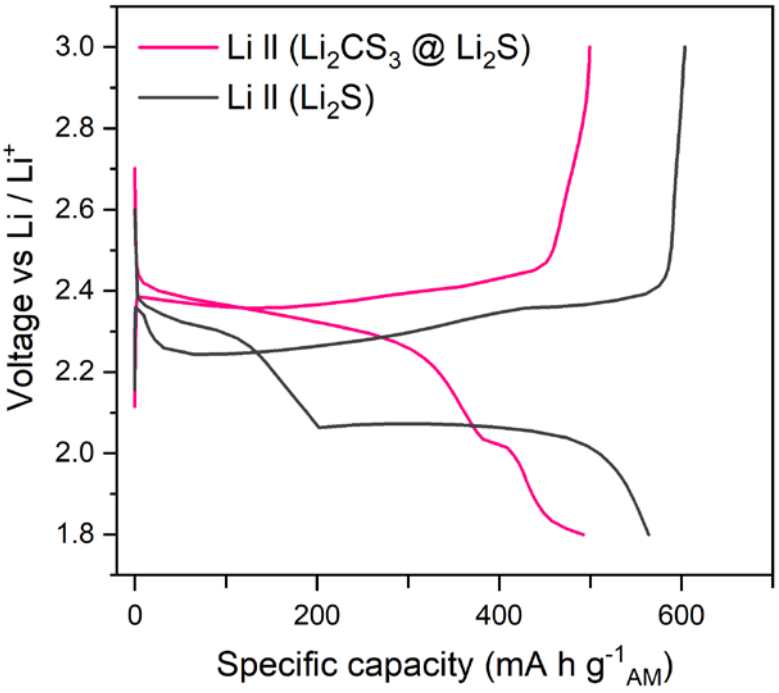

Figure S8. Charge-discharge curves at the 2nd cycle of Li || (Li_2CS_3 @ Li_2S) and Li || (Li_2S) half cells at C/5 rate.

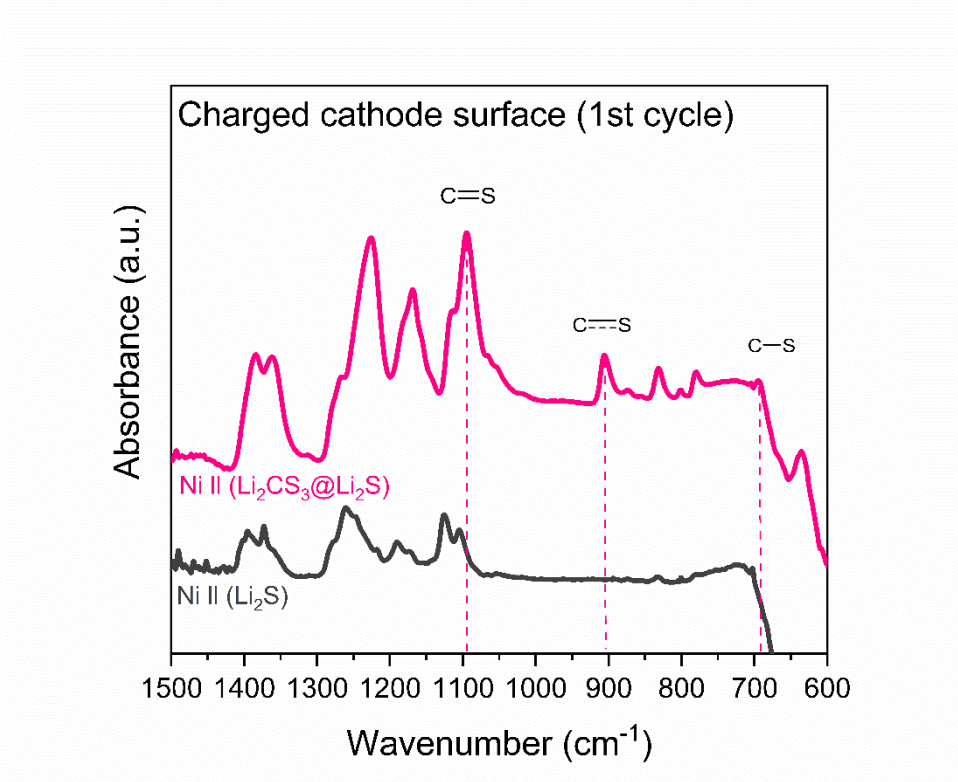

Figure S9. FTIR spectra of Ni || (Li_2CS_3 @ Li_2S) and Ni || (Li_2S) charged cathode.

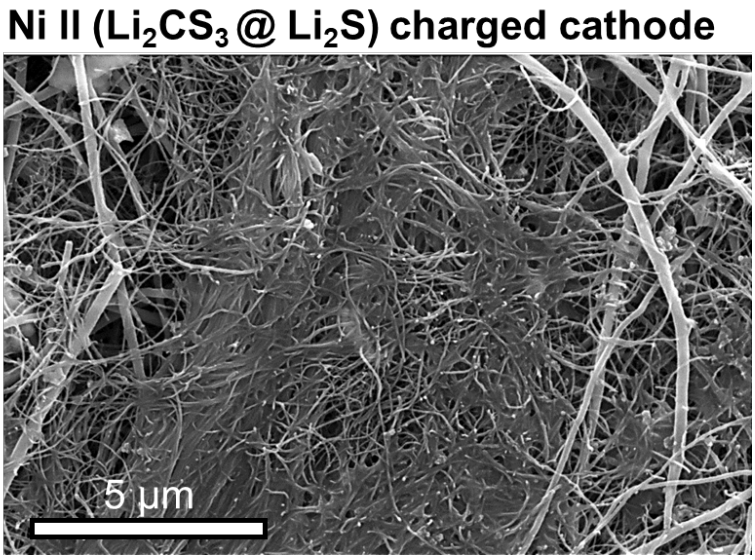

Figure S10. SEM image of Ni || (Li_2CS_3 @ Li_2S) charged cathode.

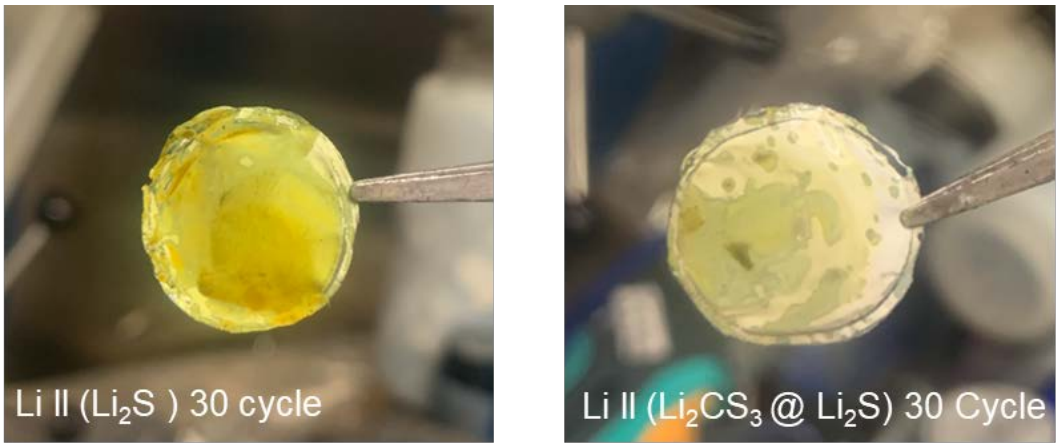

Figure S11. Comparison of the colors of the separators from Li || (Li2S) and Li || (Li2CS3 @ Li2S) cells after 30 cycles.

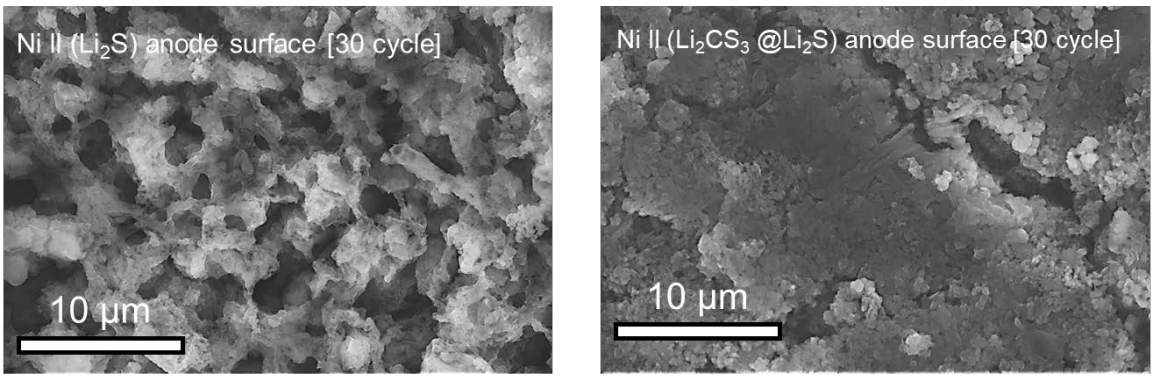

Figure S12 High magnification SEM images of the anodes from Ni || (Li_2S) and Ni || (Li_2CS_3 @ Li_2S) cells after 30 cycles.

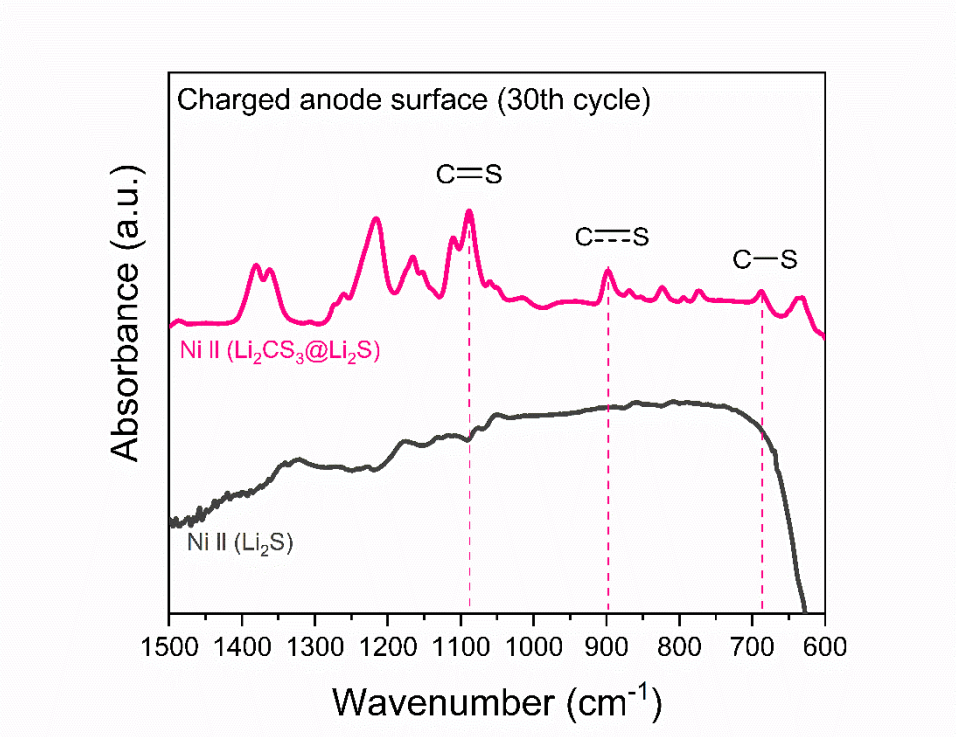

Figure S13. FTIR spectra of the anodes from Ni || (Li_2CS_3 @ Li_2S) and Ni || (Li_2S) cells after 30 cycles.

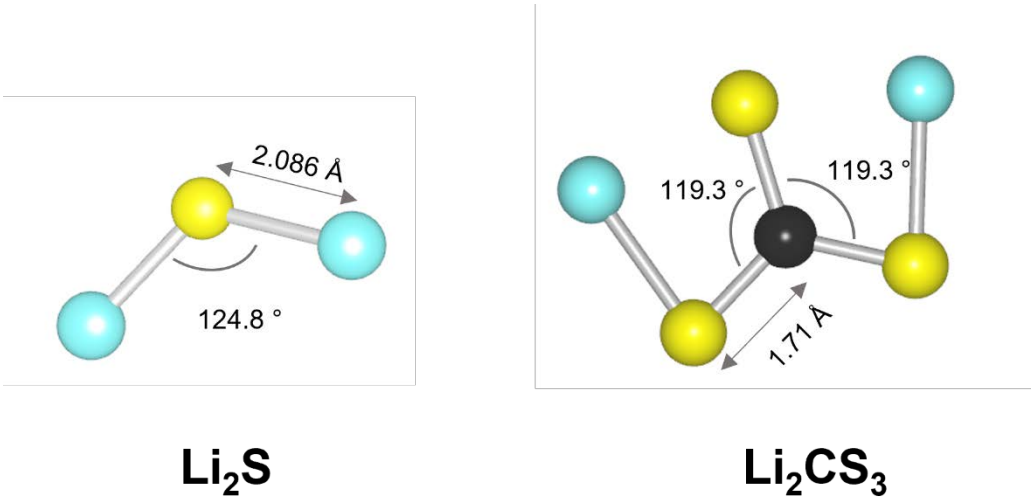

Figure S14. Relaxed structure of Li_2S and Li_2CS_3.